Structural determinants of water permeation through aquaporin-1

Kazuyoshi Murata*†, **Kaoru Mitsuoka**†‡, **Teruhisa Hirai**†‡, **Thomas Walz**§, **Peter Agre**‖, **J. Bernard Heymann**¶, **Andreas Engel**¶ **& Yoshinori Fujiyoshi**‡

* *National Institute for Physiological Sciences, Okazaki 444-8585, Japan*
‡ *Department of Biophysics, Faculty of Science, Kyoto University, Kitashirakawa, Sakyo-ku, Kyoto, 606-8502, Japan*
§ *Department of Cell Biology, Harvard Medical School, 240 Longwood Avenue, Boston, Massachusetts, 02115-5730, USA*
‖ *Departments of Biological Chemistry and Medicine, Johns Hopkins University School of Medicine, Baltimore, Maryland 21205-2185, USA*
¶ *M. E. Müller-Institute for Microscopy at the Biozentrum, University of Basel, Basel CH-4056, Switzerland*
† *These authors contributed equally to this work.*

Human red cell AQP1 is the first functionally defined member of the aquaporin family of membrane water channels. Here we describe an atomic model of AQP1 at 3.8 Å resolution from electron crystallographic data. Multiple highly conserved amino-acid residues stabilize the novel fold of AQP1. The aqueous pathway is lined with conserved hydrophobic residues that permit rapid water transport, whereas the water selectivity is due to a constriction of the pore diameter to about 3 Å over a span of one residue. The atomic model provides a possible molecular explanation to a longstanding puzzle in physiology—how membranes can be freely permeable to water but impermeable to protons.

The cells of all life forms are surrounded by a membrane and filled with water. Although simple lipid bilayers exhibit limited water permeability, membranes of red cells, cells in renal proximal tubules and in certain other tissues are extremely permeable to water. Water-selective membrane channel proteins were predicted in these tissues to explain the high water permeability (low activation energy) and reversible inhibition by mercuric ions[1]. AQP1 was first identified as an integral membrane protein in red blood cells and renal proximal tubules[2,3], where it functions as a water-selective membrane pore[4]. The aquaporin water channel family is found throughout nature and is involved in numerous physiological processes[5].

Biological membranes exquisitely control the entry and exit of ions from cells. Aquaporins have to be highly specific for water to prevent other solutes and ions from also crossing the membrane. Protons present a particularly difficult challenge, because the positive charge of a proton (H_3O^+) can move along a column of water by hydrogen bond exchange[6]. Proton fluxes across cellular membranes drive physiological processes, such as membrane fusion, vesicular transport, solute transport and ATP synthesis.

The first insight into the structure and function of AQP1 came from sequence analyses and expression studies in *Xenopus laevis* oocytes. The AQP1 monomer contains 269 amino-acid residues[3], which form two tandem repeats of three membrane-spanning α-helices with amino- (N-) and carboxy- (C-) termini located on the cytoplasmic side of the membrane[7–9]. In the hourglass model[10], connecting loops B (cytoplasmic) and E (extracellular) each contain the consensus motif Asn-Pro-Ala and dip into the membrane from the opposite sides where they overlap, forming a single transmembrane aqueous pathway through each subunit of the AQP1 tetramer[11,12]. Reconstitution of highly purified human red cell AQP1 into well-ordered membrane crystals has permitted definition of AQP1 structure at increasingly higher levels of resolution[13–16]. Here we present an atomic model of AQP1 and discuss the structural basis for water selectivity.

Density map from electron crystallography

The two-dimensional (2D) crystals of AQP1 used in this study were of limited size, typically 1 µm in diameter, making high-resolution data collection difficult especially at highly tilted conditions, whereas diffraction patterns from non-tilted crystals showed clear spots to a higher resolution than 3.5 Å. A helium-cooled electron

microscope[17,18] helped us to improve the resolution of our structural analysis by reducing the effects of radiation damage as well as by enabling us to record a large number of electron micrographs and diffraction patterns. By selecting only images and electron diffraction patterns taken from well-ordered crystals, as judged by image analysis and comparison with a preliminary merged three-dimensional (3D) data set; we calculated a 3D density map at a resolution of 3.8 Å in the membrane plane and 4.6 Å normal to the membrane (Table 1).

The AQP1 monomer contains six tilted, membrane-spanning α-helices forming a right-handed bundle[13,16,19]. The 3.8 Å map clearly resolves protrusions corresponding to individual side chains on membrane-spanning α-helices; these permitted unambiguous assignment of the α-helical structure. We established the quality and correctness of the final atomic model by alignment of 164 aquaporin sequences[20], computational fitting of α-helical fragments to the 4.5 Å map[21], and by mutagenesis[10].

The quality of our crystallographic data was relatively poor, as seen in the phase residual of 40.3° (Table 1). Nevertheless, the phase

Table 1 Electron crystallographic data

Two-dimensional crystals	
Layer group	p42₁2
Unit cell	$a = b = 96.0$ Å
Thickness	100 Å (assumed)
Electron diffraction	
Number of diffraction patterns merged	135
Resolution	3.8 Å (in membrane plane)
	4.4 Å (normal to membrane plane)
$R_{Friedel}$	44.0%
R_{merge}	49.5% (54.3% from 4.3 to 3.8 Å)
Observed amplitudes to 3.8 Å	85.254
Maximum tilt	61.1°
Fourier space sampled	88.0%
Phase determination by image processing	
Processed images	103
Resolution	3.8 Å (in membrane plane)
	4.6 Å (normal to membrane plane)
Average phase residual	40.3° (58.2° from 4.3 to 3.8 Å)
Observed phases to 3.8 Å	24,181
Maximum tilt	62.0°
Fourier space sampled*	54.0%
Crystallographic refinement	
Crystallographic R factor (96 Å to 3.8 Å)	39.9%
Free R factor (96 Å to 3.8 Å)	41.7%

* Only reflections with a figure of merit over 0.5 were included.

residual corresponds to a figure of merit of 0.76, similar or better than the initial phases ordinarily determined by X-ray crystallography. The quality of the map was sufficient for model building (Fig. 1), although surface loops were less well defined, so their positions represent the most likely assignment.

Protein fold of the AQP1 monomer

The order of α-helices in the AQP1 monomer was previously unknown. Beginning at the four-fold axis of the tetramer, the helices are arranged: 2-1-3 (first repeat), 5-4-6 (second repeat). In the first repeat, helices 1 and 2 run almost parallel to each other, and are tilted to approximately the same angle. Helix 3 is oriented almost perpendicular to the axis roughly defined by the top-on view of the first two helices. The arrangement of the first and second repeat exhibits a pseudo two-fold axis running parallel to the membrane plane at the centre of the molecule (Fig. 2a–c).
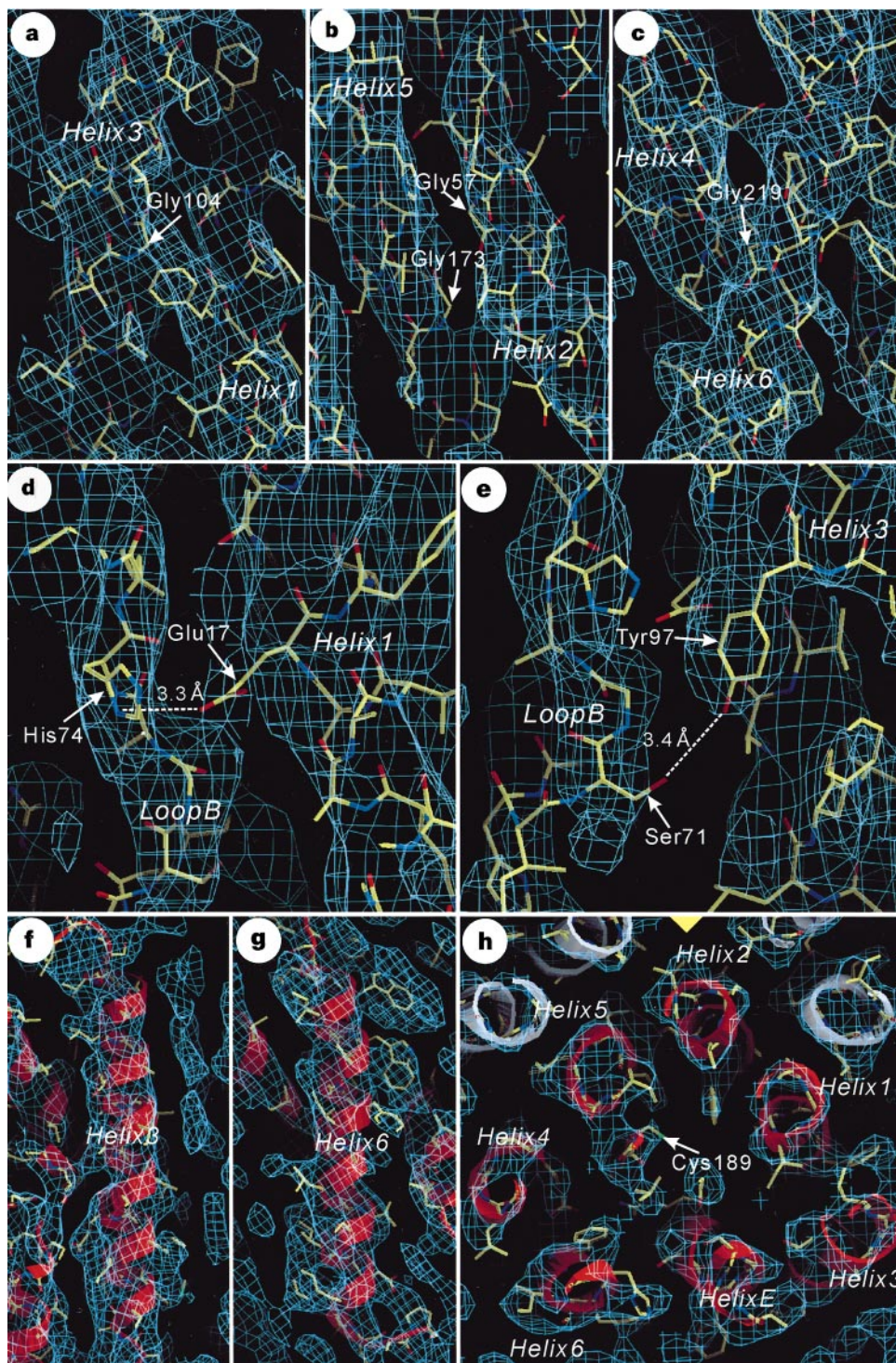

Figure 1 Representative areas of the AQP1 potential map with the fitted atomic model. **a**, Interaction of helices 1 and 3; the arrow depicts Gly 104. **b**, Ridges into grooves structure for the stable interaction between helices 2 and 5; the arrows show Gly 57 and Gly 173. **c**, Interaction of helices 4 and 6; the arrow indicates Gly 219. **d**, Ion pair formed by Glu 17 and His 74. **e**, Hydrogen bonding between Ser 71 and Tyr 97 (one of the noisiest parts of the potential map at the membrane surface). **f**, **g** Density for helix 3 and the corresponding helix 6. A cluster of large protrusions were assigned to aromatic residues Trp 210, Phe 212, and Trp 213 in helix 6; no bulky protrusions are found in the density assigned for helix 3. **h**, Section through the monomer close to Cys 189 in loop E. The yellow triangle indicates the four-fold axis of the AQP1 tetramer.

The short N terminus of AQP1 is located on the cytoplasmic side of the membrane (Fig. 3). Helix 1 then crosses the membrane and is connected to helix 2 by the extended extracellular loop A with the glycosylation site Asn 41 forming a weak density in our map. Helix 2 returns back through the membrane adjacent to helix 1 near the four-fold axis of the AQP1 tetramer. At the cytoplasmic end of helix 2, loop B folds back into the membrane positioning the Asn-Pro-Ala motif midway through the membrane. Following the Asn-Pro-Ala motif, loop B forms the short pore helix HB located adjacent to helix 6. At the cytoplasmic surface farthest from the four-fold axis, HB emerges from the membrane and connects to helix 3, which crosses the membrane adjacent to helix 1 and termi-

nates on the extracellular surface. The first and second repeat of each monomer are connected by the 18-residue loop C which spans the entire extracellular surface of the monomer joining helix 3 to helix 4 (Fig. 2a and b). Oriented opposite to the first repeat, the second repeat begins at the extracellular surface as helix 4 which crosses the membrane and is connected to helix 5 by the short loop D near the four-fold axis. Helix 5 returns back through the membrane between helix 4 and helix 2 to the extracellular surface. Loop E folds back into the membrane from the extracellular side, and the Asn-Pro-Ala motif is positioned near the centre of the molecule where it crosses the Asn-Pro-Ala motif in loop B at a right angle (Fig. 2c, 4a and c), and forms the short pore helix HE. Helix 6 crosses the membrane adjacent to

Figure 2 Ribbon representations of the AQP1 fold depicting the six membrane-spanning helices, the two pore helices, and the connecting loops in different colours. **a**, End-on view from the extracellular surface; **b**, side view; **c**, end-on view from the cytoplasmic surface. **d**, Cylinder model of the AQP1 tetramer; end-on view from the extracellular surface; **e**, side view. Yellow diamonds and yellow dotted line indicate the four-fold axis of the AQP1 tetramer. Dotted lines and spindle in white show the pseudo two-fold axis of the AQP1 monomer. Grey bands indicate the surface of the lipid bilayer. **a**–**c** were prepared with MOLSCRIPT[45] and Raster 3D[46].

helix 4, with the C-terminus emerging on the cytoplasmic side of the membrane (Fig. 3).

Three large helical crossing angles stabilize the right-handed coiled-coil interactions (Table 2). Helices 1 and 3 (36.7°), helices 4 and 6 (40.9°), and helices 2 and 5 (28.5°) all have highly conserved glycine residues at the contact sites. The glycine residues at the contact region, Gly 104 for helices 1 and 3, Gly 219 for helices 4 and 6, are shown in Fig. 1a and 1c. The crossing of helix 2 (first repeat) and helix 5 (second repeat) is maintained by interactions involving highly conserved residues Gly 57 and Gly 173 (Fig. 1b). The fitting of ridges into grooves in helices 2 and 5 lock the two AQP1 helical bundles together closely at the four-fold axis of the tetramer, opposite to the site where HB and HE interact with helices 6 and 3 (Fig. 2a). The conserved glycines[20] in helices 3 and 6 reveal the GlyxxxGly motif that is a framework for transmembrane helix-helix association[22] (Ala 100, Gly 104, Ala 108 in helix 3, Gly 215, Gly 219, Ala 223 in helix 6; glycine can sometimes be replaced by alanine in the motif). Thus, the α-helices in both repeats are held together near the interior and exterior surfaces of the monomer. Gly 82 in pore helix HB forms the contact site with helix 6 and Gly 198 in pore helix HE interacts with helix 3.

Additional highly conserved residues are concentrated in and around the two functional loops B and E that are closely positioned in the interior of the monomer[20]. Loops B and E are held together by van der Waals interactions between the prolines in the two Asn-Pro-Ala motifs (Pro 77 and Pro 193) that cross each other at an angle of approximately 90° (Fig. 4a and c). The asparagines in the Asn-Pro-Ala motifs cap the N-terminal end of the pore helices by hydrogen bonding with the main-chain NH groups at Val 79 and Arg 195. The positions of functional loops B and E are stabilized through ion pairs and hydrogen bonds. His 74 (loop B) forms an ion pair with the conserved Glu 17 (helix 1) anchoring the position of pore loop B (Fig. 1d), whereas Arg 195 in pore helix HE is connected by a salt bridge to the conserved Glu 142 (helix 4). The density for Arg 195 is less clear and could be pointing towards the membrane surface; however, this possibility seems to be very unlikely because of the conservation of this arginine in the aquaporin family. These ion pairs are stabilized by conserved polar residues that surround them within the membrane, Thr 80, Gln 101 and Ser 196. The positions of the NH groups in the main chain of the pore loops are stabilized by hydrogen bonds to highly conserved threonine residues, Thr 21

(helix 1) and Thr 146 (helix 4). In addition, the side chain of Ser 71 (loop B) forms a hydrogen bond with Tyr 97 (helix 3), further stabilizing the position of this loop (Fig. 1e).

AQP1 tetramer

AQP1 is a homotetramer (Fig. 2d and e). Stability may result from accommodation of each monomer as a tight-fitting wedge within the tetramer. The relative insolubility of AQP1 in certain detergents[12] indicates that surrounding lipids may be tightly attached. Sufficient space lies between adjacent tetramers in the 2D membrane crystals to accommodate at least one lipid molecule that may be important in crystal formation. Amino-acid residues interacting with the acyl chains of the lipids in the tetramer are found in helices 3 and 6 and pore helices HB and HE, which reside at the exteriors of the monomers.

Each monomer interacts with two neighbouring monomers through membrane-spanning α-helices. Helices 1 and 2 form left-handed coiled-coil interactions with helices 4 and 5 of the neighbouring monomer with crossing-angles of 48.5° and 48.0°. Helix 1 also interacts with helix 5 of the adjacent monomer at the extracellular surface, whereas helix 2 interacts with helix 4 of the adjacent monomer at the cytoplasmic surface. These interactions are probably stabilized by a network of hydrogen bonds between residues Ser 59, Thr 62, and Gln 65 (helix 2) with residues Gln 148, Cys 152, and Thr 156 (helix 4 of the adjacent monomer).

Interactions between loops may also contribute to tetramer stability. Loops A in the four monomers surround the four-fold axis of the tetramer on the extracellular surface, whereas loops D surround the axis on the cytoplasmic surface. The 3.8-Å structure

Table 2

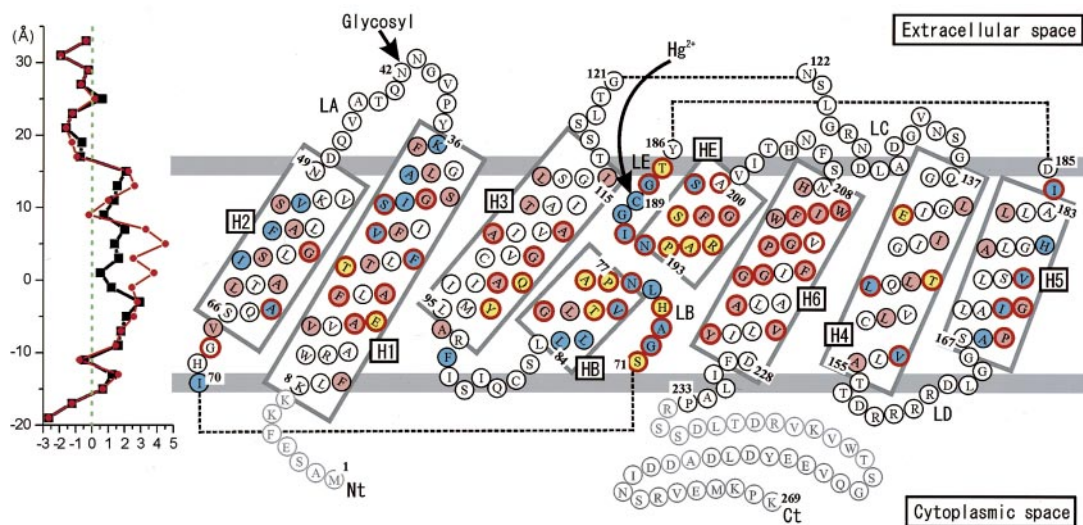|	Start	End	Tilt angle to membrane normal (degree)	Angle between two helices (degree)
Helix 2	49	66	23.7	17.5 (h2 to h1)
Helix 1	8	36	27.2	36.7 (h1 to h3)
Helix 3	95	115	39.9	9.0 (h3 to hB)
Helix B	77	84	34.2	33.9 (hB to h6)
				42.4 (hE to h3)
Helix E	193	200	37.6	4.9 (hE to h6)
Helix 6	208	228	33.5	40.9 (h6 to h4)
Helix 4	137	155	24.3	5.8 (h4 to h5)
Helix 5	167	183	24.8	28.5 (h2 to h5)

Figure 3 Schematic representation of AQP1 topology and hydropathy. Secondary structural elements in AQP1 indicating structurally important amino-acid residues: those that face the inside of the aqueous pore in the membrane (blue); highly conserved residues (thick red circles); residues stabilizing loop-associations (yellow); contact points for helix-helix interaction (pink). The surfaces of the lipid bilayer are represented by grey bands. The density map did not allow us to trace the seven N- and 36 C-terminal amino-acid residues (grey). On the left side, the hydrophobicity of the molecular surface of AQP1 is shown, indicating the boundaries of the lipid bilayer. Hydropathy plots were calculated from all amino-acid residues (red) and from residues not buried (black).

reveals a protrusion from the extracellular surface of the AQP1 tetramer, whereas the cytoplasmic side forms a shallow depression (Fig. 2b and e). The N terminus extends from the periphery of the tetramer on the cytoplasmic side in close proximity to the C terminus of the adjacent monomer.

Helices 2 and 5 incline towards the four-fold axis at the extracellular side and the cytoplasmic side of the membrane (Fig. 2d). The narrowest parts about the four-fold axis reside close to both membrane surfaces near Val 50 (helix 2) and Leu 170 (helix 5). At this level, the gap in the space-filling model without hydrogen atoms has a diameter of about 3.5 Å. At its widest, the diameter of the gap is approximately 8.5 Å, which is insufficient to accommodate a lipid molecule. The hydrophobic environment, however, suggests that this space is filled with a hydrophobic molecule. Thus, the space at the four-fold axis of the tetramer does not form a pathway for water.

Structure of the aqueous pore

The critical function of AQP1 is its exceptional water permeability, 3×10^9 molecules per monomer per second[23–25]. As predicted by the hourglass model[10], loops B and E interact with each other through

their Asn-Pro-Ala motifs, forming part of the surface of the aqueous pore (Fig. 4a and b). Helices 2 and 5 together with the C-terminal halves of helices 1 and 4 form the remaining surface of the pore (blue residues, Fig. 3). The 3 Å diameter of the narrowest part of the pore measured by van der Waals distance, determined from a carbon–carbon distance of 6.5 Å, is only slightly larger than the 2.8 Å diameter of a water molecule (Fig. 4a). Although the span of this constriction is only one amino-acid residue, this would block passage of larger solutes and ions. Unlike the potassium channel[26], AQP1 does not contain a structure to liberate ions from their hydration shell. Thus, the atomic model of AQP1 is consistent with biophysical measurements that showed no solute, ion or proton permeability[25,27,28].

The 3 Å constriction in the pore is located in the centre of the membrane just beside the region where loops B and E interact with each other. Ile 60 (helix 2), Phe 24 (helix 1), Leu 149 (helix 4) and Val 176 (helix 5) form a hydrophobic surface lining the inside of the pore adjacent to Asn 76 and Asn 192 of the Asn-Pro-Ala motifs (Fig. 4a and b). Two histidines are located within 5 Å of the pore constriction. His 74 is highly conserved and forms an ion pair with Glu 17 (Fig. 1d). His 180 is conserved in water-selective
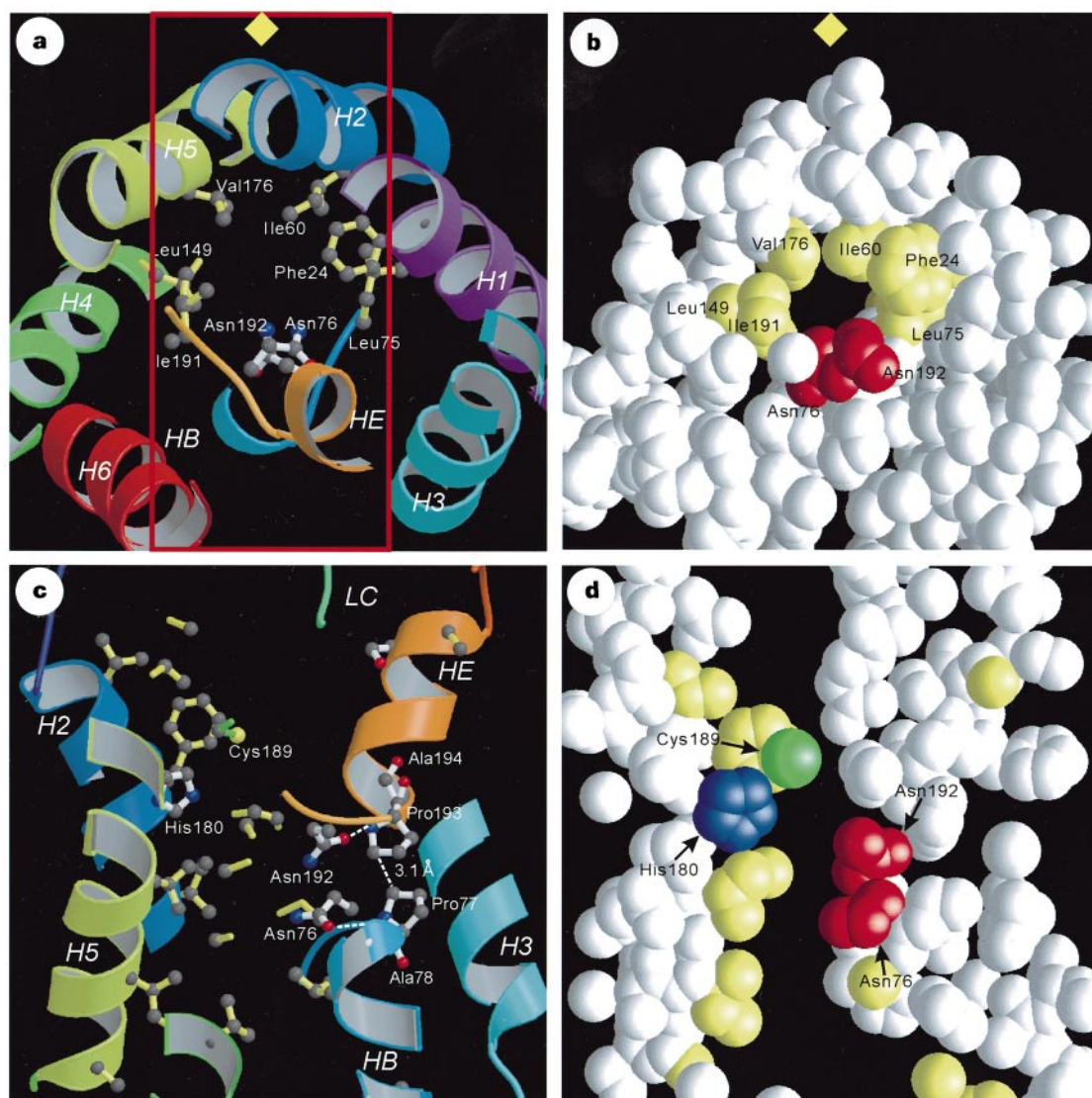

Figure 4 Ribbon and space-filled diagrams representing the structure of the aqueous pore in AQP1. **a**, Section cut parallel to the plane of the membrane through the centre of the AQP1 monomer showing the constriction of the pore. **b**, Space-filled model of the same view as **a** showing the pore diameter. **c**, Section cut across the membrane as outlined by red rectangle-lines perpendicular to the plane in **a**, showing the side view of the interior of the AQP1 pore. **d**, Space-filled model of the same view as in panel **c** showing the widening (top and bottom) and constriction of the pore (centre). Yellow diamonds in **a** and **b** show the four-fold axis of the AQP1 tetramer. Side chains facing the inside of the aqueous pore are indicated: hydrophobic side chains at the pore constriction (yellow); Asn 76 and Asn 192 (red); cysteine (green); His 180 (blue). **a**–**d** were prepared with MOLSCRIPT[45] and Raster 3D[46].

members of the aquaporin family but is usually replaced by glycine in homologues permeated by glycerol[20], suggesting that it plays a specific role in water conductance. Hydrophobicity of the inner pore surface and small axial dimension (5 Å) of the constriction are probably of crucial importance for facilitating the exceptionally high water permeability of AQP1.

The free sulphhydryl of Cys 189 in loop E projects into the pore from the extracellular side of the narrowing (Figs 1h, 3, 4c and d) where inhibition of AQP1 water permeation by mercury[29,30] must result from occlusion of the aqueous pathway. As expected for a symmetrical structure, Ala 73, the corresponding residue in loop B, resides at a comparable location on the cytoplasmic side of the narrowing, explaining the inhibition of the double mutant Cys 189 Ser, Ala 73 Cys by mercury[10].

Permeation by water but not protons

As studied in detail with gramicidin A, water can readily cross cell membrane as a continuous unbroken column of molecules within an open pore. This single-file hydrogen-bonded chain of water molecules conducts protons with great efficiency[6]. In contrast, no proton conductance was detected in AQP1 (ref. 25), so the pore must prevent their passage. The mechanism that prevents transfer of protons during rapid water permeation remains an important unanswered question in the structural biology of aquaporins. Blocking proton transfer is believed to require interruption of the continuous chain of hydrogen bonds along a single file of water by hydrogen-binding sites at the pore surface[6]. The hydrogen-bonding energy is about 3 kcal (ref. 31), close to the activation energy for the passage of water through AQP1 (ref. 24), suggesting that breakages of hydrogen bonds are involved in the water flow.

The pore helices HB and HE and the neighbouring Asn residues in the two Asn-Pro-Ala motifs may be critical elements for this process. Short pore helices were also identified in the atomic structure of the potassium channel from *Streptomyces lividans*[26]. The C-termini of those pore helices point into the large aqueous cavity surrounded by the membrane-spanning helices. In contrast, the AQP1 pore helices are oriented in the opposite direction, the C-termini facing out. Due to the positive electrostatic field generated by the dipole moments of the pore helices in AQP1, the oxygen atom in a water molecule coming close to the membrane centre orients to the side of the Asn-Pro-Ala motif (Fig. 5a). We note that the shape of the AQP1 pore is the opposite of the pore shape formed by the potassium channel[26], having a constriction in the centre of the membrane and wide openings at the membrane surfaces. This constriction results in a high dielectric barrier that repels ions, while allowing penetration of neutral solutes.

The pore helices HB and HE are held in the middle of the membrane by van der Waals interactions between the Pro residues of the two Asn-Pro-Ala motifs. Our atomic model suggests hydrogen bonds between the main chain NH groups and the carbonyl groups of the two asparagine residues in the Asn-Pro-Ala motifs, thus capping the N-terminal end of the short pore helices. As a result, the amido groups of Asn 76 and 192 are fixed to extend into the pore at the constriction (Fig. 5). The oxygen atom of the water molecule here will form hydrogen bonds with these amido groups by changing the hydrogen-bonding partner from adjacent water molecules (Fig. 5b). This reorients the two hydrogen atoms of the water molecule at the pore constriction perpendicular to the channel axis because of the arrangement of the molecular orbital for water (Fig. 5c). Thus, the two hydrogen atoms of the water molecule are prevented from forming hydrogen bonds with adjacent water molecules in the single-file column. Because all residues near the constriction are hydrophobic, no hydrogen-bonding partners are provided by the opposite wall of the pore, giving a maximum energy cost of 3 kcal, because only one hydrogen bond relative to bulk water is affected. The water molecule in the pore constriction can form hydrogen bonds via oxygen but not through

hydrogen atoms. Thus, water molecules can permeate the pore with a minimal energy barrier, whereas transfer of protons is blocked by hydrogen-bond isolation from bulk water (H-bond isolation mechanism). Because our analyses were restricted to the resolution of 3.8 Å, no water molecules could be observed. Higher-resolution structural studies may prove our hypothesis if the occupancy of water molecules at the pore constriction is sufficiently high.

The aquaporin family

Although our atomic model explains several key features of the AQP1 pore, many open questions remain concerning other members of the aquaporin family. For example, how can the same protein fold account for the extreme water-selectivity of AQP1 and the broad substrate specificity of AQP9 (ref. 32)? How can aquaglyceroporins allow passage of glycerol but be less permeable to water than AQP1? How do anions pass through AQP6 (ref. 33)? What are the molecular mechanisms for regulation of several aquaporins?

The atomic model provides a precedent for modelling other aquaporins by carefully threading their amino-acid sequences along the main-chain fold of AQP1. The models can then be used to make predictions about which residues are important for pore selectivity. Site-directed mutagenesis of key residues in the atomic model of AQP1 will permit assessment of their functional importance. This should open new avenues for investigating the structural determinants of pore specificities in other members of the aquaporin family. Although low-resolution density maps of other aquaporins will provide guidance for modelling, the atomic structures are needed to bring unambiguous identification of the molecular determinants.

Note added in proof: The structure of the glycerol facilitator (GlpF), an aquaglyceroporin from *E. coli*, has now been determined[47]. □

Methods

Data collection

Two-dimensional crystals of AQP1 were produced as described previously[23], and prepared
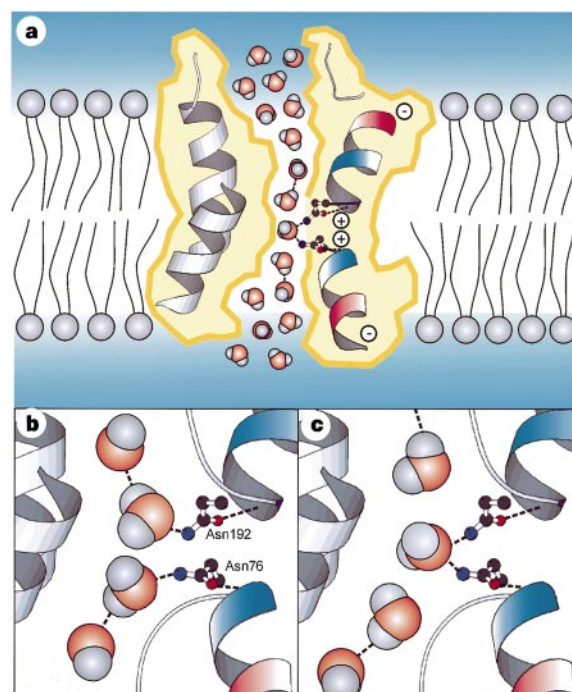
Figure 5 Schematic representations explaining the mechanism for blocking proton permeation of AQP1. **a**, Diagram illustrating how partial charges from the helix dipoles restrict the orientation of the water molecules passing through the constriction of the pore. **b** and **c** Diagram illustrating hydrogen bonding of a water molecule with Asn 76 and/or Asn 192, which extend their amido groups into the constriction of the pore. The ribbon and ball-stick models in this figure were prepared with MOLSCRIPT[45].

for electron cryomicroscopy on thin carbon-coated molybdenum grids using trehalose as embedding medium at a final concentration of 3%[16,34]. Electron micrographs and diffraction patterns were recorded with a JEM 3000SFF electron microscope equipped with a liquid-helium stage[17,18] and a field-emission electron source using an acceleration voltage of 300 kV. Electron micrographs recorded under low-dose conditions ($< 20\, e^- \mathring{A}^{-2}$) were digitized with a LeafScan45 scanner (Scitex)[35] for image processing; electron-diffraction patterns were collected with a 2K slow-scan charge-coupled device (CCD) camera (Gatan)[36]. Electron-diffraction patterns and images were processed with a modified version of the MRC image processing programs[37]. Electron-diffraction patterns (173) tilted up to 61.1° were analysed to calculate amplitudes using an additional background-correction step[38]. Images were computationally unbent and corrected for the contrast-transfer function[39]. Images (124) tilted up to 62.0° were averaged to generate a merged-phase data set. The final three-dimensional potential map was produced with the CCP4 programs[40] from merged amplitudes and phases with figures of merit above 0.5.

A problem for the data collection arose from the relatively small size and lattice defects of the AQP1 2D crystals that prevented collection of data of very high resolution. Substantially more data were collected and processed than needed for calculation of a 3D density map at a resolution of 3.8 Å. Images and diffraction patterns were excluded from the final analysis if they did not significantly improve the statistics. Thus, our final data set includes 135 electron diffraction patterns (providing structure factor amplitudes) and 103 images (providing experimental phases) collected from specimens at tilt angles up to 60°. Statistics of our electron-crystallographic analysis of the AQP1 structure are summarized in Table 1.

Model building

The atomic model was built using the program O (ref. 41). Conventionally constrained (positional) refinement of the initial hand-built model was performed with the program X-PLOR[42] without simulated annealing, with phase and amplitude constraints. The moderate resolution and the relatively poor quality of our electron-crystallographic data (Table 1) added to the challenge of building an atomic model for AQP1. The map is of a quality similar to initial non-refined electron-density maps determined by X-ray crystallography of proteins with large relative molecular mass. Furthermore, most of the densities in the membrane region of the 3D map were clearly defined. Only the extramembranous regions of the proteins contained some persistent ambiguities.

Each tandem repeat of AQP1 contains three membrane-spanning α-helices. The second half of the protein (helices 4–6) is incorporated into the membrane in an orientation opposite to the first half of the protein (helices 1–3). Thus, the two halves of the protein are related to each other by a pseudo two-fold axis that runs parallel to the membrane plane[13] (Fig. 2a–c). This symmetry of the AQP1 structure constituted a major difficulty during the actual model building, because each density in the 3D map could be assigned to either of two possible helices in the AQP1 molecule—a helix in the first tandem repeat or the corresponding helix in the second tandem repeat. Of note, the densities for helices 3 and 6 were clearly distinguishable, because helix 6 contains a cluster of aromatic residues (Phe 206, His 209, Trp 210, Phe 212 and Trp 213) not present in helix 3 (Fig. 1f and g), whereas the accurate assignment of individual residues was difficult. Similarly, several bulky side chains in pore helix HB that are missing from pore helix HE enabled us to distinguish the two tandem repeats and provided a starting point for the model building. Our assignment is also supported by the sidedness of AQP1 and AqpZ (ref. 43) determined by atomic force microscopy[44].

PROCHECK was used to calculate a Ramachandran plot for our atomic model of residues 8–233 (missing seven N-terminal and 36 C-terminal amino-acid residues). 70 per cent of residues fell into the most favourable locations, whereas only five amino-acid residues from connecting-loop domains fell into the generously allowed regions.

1. Macey, R. I. & Farmer, R. E. I. Inhibition of water and solute permeability in human red cells. *Biochem. Biophys. Acta* **211**, 104–106 (1970).
2. Denker, B. M., Smith, B. L., Kuhajda, F. P. & Agre, P. Identification, purification, and partial characterization of a novel Mr 28,000 integral membrane protein from erythrocytes and renal tubules. *J. Biol. Chem.* **263**, 15634–15642 (1988).
3. Preston, G. M. & Agre, P. Isolation of the cDNA for erythrocyte integral membrane protein of 28 kilodaltons: Member of an ancient channel family. *Proc. Natl Acad. Sci. USA* **88**, 11110–11114 (1991).
4. Preston, G. M., Carroll, T. P., Guggino, W. B. & Agre, P. Appearance of water channels in *Xenopus* oocytes expressing red cell CHIP28 protein. *Science* **256**, 385–387 (1992).
5. Heymann, J. B. & Engel, A. Aquaporins: Phylogeny, structure and physiology of water channels. *News Physiol. Sci.* **14**, 187–193 (1999).
6. Pomes, R. & Roux, B. Structure and dynamics of a proton wire: a theoretical study of H$^+$ translocation along the single-file water chain in the gramicidin A channel. *Biophys. J.* **71**, 19–39 (1996).
7. Wistow, G., Pisano, M. & Chepelinsky, A. Tandem sequence repeats in transmembrane channel proteins. *Trends Biochem. Sci.* **16**, 170–171 (1991).
8. Reizer, J., Reizer, A. & Saier, M. J. The MIP family of integral membrane channel proteins: sequence comparisons, evolutionary relationships, reconstructed pathway of evolution, and proposed functional differentiation of the two repeated halves of the proteins. *Crit. Rev. Biochem. Mol. Biol.* **28**, 235–257 (1993).
9. Preston, G. M., Jung, J. S., Guggino, W. B. & Agre, P. Membrane topology of aquaporin CHIP. Analysis of functional epitope-scanning mutants by vectorial proteolysis. *J. Biol. Chem.* **269**, 1668–1673 (1994).
10. Jung, J., Preston, G. M., Smith, B., Guggino, W. & Agre, P. Molecular structure of the water channel through aquaporin CHIP. The hourglass model. *J. Biol. Chem.* **269**, 14648–14654 (1994).
11. van Hoek, A. N. *et al.* Functional unit of 30 kDa for proximal tubule water channels as revealed by radiation inactivation. *J. Biol. Chem.* **266**, 16633–16635 (1991).
12. Smith, B. L. & Agre, P. Erythrocyte M$_r$ 28,000 transmembrane protein exists as a multisubunit oligomer similar to channel proteins. *J. Biol. Chem.* **266**, 6407–6415 (1991).
13. Cheng, A., van Hoek, A. N., Yeager, M., Verkman, A. S. & Mitra, A. K. Three-dimensional organization of a human water channel. *Nature* **387**, 627–630 (1997).
14. Li, H., Lee, S. & Jap, B. K. Molecular design of aquaporin-1 water channel as revealed by electron crystallography. *Nature Struct. Biol.* **4**, 263–265 (1997).
15. Walz, T., Smith, B., Agre, P. & Engel, A. The three-dimensional structure of human erythrocyte aquaporin CHIP. *EMBO J.* **13**, 2985–2993 (1994).
16. Walz, T. *et al.* The three-dimensional structure of aquaporin-1. *Nature* **387**, 624–627 (1997).
17. Fujiyoshi, Y. *et al.* Development of a superfluid helium stage for high-resolution electron microscopy. *Ultramicroscopy* **38**, 241–251 (1991).
18. Fujiyoshi, Y. The structural study of membrane proteins by electron crystallography. *Adv. Biophys.* **35**, 25–80 (1998).
19. Mitsuoka, K. *et al.* The structure of aquaporin-1 at 4.5 Å resolution reveals short α-helices in the center of the monomer. *J. Struct. Biol.* **128**, 34–43 (1999).
20. Heymann, J. B. & Engel, A. Structural clues in the sequences of the aquaporins. *J. Mol. Biol.* **295**, 1039–1053 (2000).
21. De Groot, B. L. *et al.* The fold of human aquaporin 1. *J. Mol. Biol.* (in the press).
22. Russ, W. P. & Engelman, M. The GxxxG motif: a framework for transmembrane helix-helix association. *J. Mol. Biol.* **296**, 911–919 (2000).
23. Walz, T., Smith, B., Zeidel, M., Engel, A. & Agre, P. Biologically active two-dimensional crystals of aquaporin CHIP. *J. Biol. Chem.* **267**, 1583–1586 (1994).
24. Zeidel, M. *et al.* Reconstitution of functional water channels in liposomes containing purified red cell CHIP28 protein. *Biochemistry* **31**, 7436–7440 (1992).
25. Zeidel, M. *et al.* Ultrastructure, pharmacologic inhibition, and transport selectivity of aquaporin channel-forming integral protein in proteoliposomes. *Biochemistry* **33**, 1606–1615 (1994).
26. Doyle, D. A. *et al.* The structure of the potassium channel: Molecular basis of K$^+$ conduction and selectivity. *Science* **280**, 69–77 (1998).
27. Gutierrez, A. M., Gonzales, E., Echevarria, M., Hernandez, C. S. & Whittembury, G. The proximal straight tubule (PST) basolateral cell membrane water channel: Selectivity characteristics. *J. Membr. Biol.* **143**, 189–197 (1995).
28. Yang, B, van Hoek, A. N. & Verkman, A. S. Very high single channel water permeability of aquaporin-4 in baculovirus-infected insect cells and liposomes reconstituted with purified aquaporin-4. *Biochemistry* **36**, 7625–7632 (1997).
29. Preston, G., Jung, J., Guggino, W. & Agre, P. The mercury-sensitive residue at cycteine 189 in the CHIP28 water channel. *J. Biol. Chem.* **268**, 17–20 (1993).
30. Zhang, R., van Hoek, A. N., Biwersi, J. & Verkman, A. S. A point mutation at cysteine 189 blocks the water permeability of rat kidney water channel CHIP28. *Biochemistry* **32**, 2938–2941 (1993).
31. Schulz, G. E. & Schermer, R. H. in *Principles of Protein Structure* (ed. Cantor, C. R.) 17–26 (Springer, New York, 1979).
32. Tukaguchi, H. *et al.* Molecular characterization of a broad selectivity neural solute channel. *J. Biol. Chem.* **273**, 24737–24743 (1998).
33. Yasui, M. *et al.* Rapid gating and anion permeability of an intracellular aquaporin. *Nature* **402**, 184–187 (1999).
34. Hirai, T. *et al.* Trehalose embedding technique for high-resolution electron crystallography: application to structural study on bacteriorhodopsin. *J. Elec. Microsc.* **48**, 653–658 (1999).
35. Mitsuoka, K., Murata, K., Kimura, Y., Namba, K. & Fujiyoshi, Y. Examination of the Leafscan 45, a line-illuminating micro-densitometer, for its use in electron crystallography. *Ultramicroscopy* **68**, 109–121 (1997).
36. Krivanek, O. L. & Mooney, P. E. Applications of slow-scan CCD camera in transmission electron microscopy. *Ultramicroscopy* **49**, 95–108 (1993).
37. Crowther, R. A., Henderson, R. & Smith, J. M. MRC image processing programs. *J. Struct. Biol.* **116**, 86–92 (1996).
38. Mitsuoka, K. *et al.* The structure of bacteriorhodopsin at 3.0 Å resolution based on electron crystallography: Implication on the charge distribution. *J. Mol. Biol.* **286**, 861–882 (1999).
39. Henderson, R., Baldwin, J. M., Downing, K. H., Lepault, J. & Zemlin, F. Structure of purple membrane from *Halobacterium halobium*: recording, measurement and evaluation of electron micrographs at 3.5 Å resolution. *Ultramicroscopy* **19**, 147–178 (1986).
40. Collaborative Computational Project No. 4. The CCP4 Suite: Programs for protein crystallography. *Acta Crystallogr. D* **50**, 760–763 (1994).
41. Jones, T. A., Zou, J. Y., Cowan, S. W. & Kjeldgaard, M. Improved methods for building protein models in electron density maps. *Acta Crystallogr. A* **47**, 110–119 (1991).
42. Brünger, A. T. X-PLOR Version 3.1-A System for X-ray Crystallography (Yale Univ. Press, New Haven/London, 1988).
43. Scheuring, S. *et al.* The aquaporin sidedness revisited. *J. Mol. Biol.* **295**, 1271–1278 (2000).
44. Scheuring, S. *et al.* High resolution AFM topographs of the *Escherichia coli* water channel aquaporin Z. *EMBO J.* **18**, 4981–4987 (1999).
45. Kraulis, P. J. MOLSCRIPT-a program to produce both detailed and schematic plots of proteins structures. *J. Appl. Crystallogr.* **24**, 946–950 (1991).
46. Merritt, E. A. & Bacon, D. J. Raster 3D: photorealistic molecular graphics. *Methods Enzymol.* **277**, 505–524 (1997).
47. Fu, D. X. *et al.* Structure of a glycerol conducting channel and the basis for its selectivity. *Science* (in the press).